Shrinking the footprints of polarization splitter-rotators with highly-birefringent molybdenum disulfide waveguides

1st Liyan Wang
CAS Key Laboratory of Nanophotonic Materials and Devices, CAS Key Laboratory of Standardization and Measurement for Nanotechnology, CAS Center for Excellence in Nanoscience
National Center for Nanoscience and Technology
Beijing, China
wangly2021@nanoctr.cn

2nd Cheng Luo
CAS Key Laboratory of Nanophotonic Materials and Devices, CAS Key Laboratory of Standardization and Measurement for Nanotechnology, CAS Center for Excellence in Nanoscience
National Center for Nanoscience and Technology
Beijing, China
Luoc2018@nanoctr.cn

3rd Debo Hu#
CAS Key Laboratory of Nanophotonic Materials and Devices, CAS Key Laboratory of Standardization and Measurement for Nanotechnology, CAS Center for Excellence in Nanoscience
National Center for Nanoscience and Technology
Beijing, China
hudb@nanoctr.cn

4th Qing Dai#
CAS Key Laboratory of Nanophotonic Materials and Devices, CAS Key Laboratory of Standardization and Measurement for Nanotechnology, CAS Center for Excellence in Nanoscience
National Center for Nanoscience and Technology
Beijing, China
daiq@nanoctr.cn

***Abstract*—A polarization splitter-rotator (PSR) based on an asymmetric directional coupler (ADC) with molybdenum disulfide (MoS_2) waveguides is proposed. Owing to the high in-plane refractive index and the extreme birefringence of MoS_2, an ultra-small cross-polarization coupling length of 6.0 μm can be achieved. At the working wavelength of 1.55 μm, this ADC-type PSR exhibits a high TM_0-to-TE_0 polarization conversion efficiency of 96.97% and a low conversion loss of 0.38 dB. Additionally, the TE_0-to-TE_0 insertion loss and cross-talk are remarkably low, measuring at 0.006 dB and -31.53 dB, respectively. We verify through simulations that the extremely high birefringence of MoS_2 is a necessity for achieving simple and ultra-compact ADC-PSR with straight waveguide geometries. This exceptional impact of extreme birefringence of MoS_2 indicates a unique and promising prospect for developing high-performance nanophotonic components based on the van der Waals on insulator (vdW-OI) configuration.**

Keywords—integrated optics, polarization management, optical anisotropy, van der Waals materials, modal birefringence

I. Introduction

Polarization splitters [1-3] and polarization rotators [4] can realize the separation and inter-conversion of orthogonally polarized transverse electric (TE) and transverse magnetic (TM) waveguide modes, alleviate the polarization dependence of the high refractive index contrast silicon-on-insulator (SOI) photonic platform, [5, 6] thus are indispensable components in integrated optical circuits based on polarization-diversity schemes.[7, 8] Compared with discrete polarization splitters and rotators, compact polarization splitter-rotator (PSR) is much more desirable for achieving high-density integration in terms of reliability and stability. [9] In recent years, great efforts have been devoted to achieving compact PSRs through innovative structure designs. Typical examples include devices based on asymmetric directional couplers (ADC), [10-14] tapers, [15-19] multi-mode interference (MMI) couplers, [20] subwavelength gratings (SWGs), [21-23] metamaterials, [24, 25] and two-dimensional material composite waveguides, [26] etc. However, the PSRs based on tapers or MMI structures are challenging to reduce in footprint to below tens of micrometers. [19] Other novel designs can achieve a size reduction to around 10 μm, at the cost of some other shortcomings, such as the manufacturing difficulty associated with the structural intricacy of SWGs, [27] the extra transmission loss induced by a hybrid plasmonic waveguide (HPW), [9] and the experimental challenge caused by embedding graphene into waveguides. [26] Therefore, an ultra-compact PSR design with a simple structure yet high performance is still urgently needed.

ADC composed of two parallel straight waveguides (SW) is a promising structure to realize compact and uncomplicated PSRs on the SOI platform. [28] However, the maximum modal birefringence of silicon waveguide on SOI is limited to 0.7 with a waveguide height of 250 nm. This fundamental restriction imposes a constraint on the compact footprint achievable for Si-based straight waveguides ADC-PSRs, confining their size to the magnitude of tens of micrometers. [11] Large optical birefringence of the waveguide material is conducive to achieving significant phase mismatch between different guided modes (modal birefringence), [27] thereby would facilitate the further miniaturization of SW-based ADC-PSRs. [28] Thanks to their layered structures, transition metal dichalcogenides (TMDs) exhibit large optical anisotropies. [29-36] Especially, molybdenum disulfide (MoS_2) with a high in-plane refractive index (over 4) [37-40] and low absorption in the communication band [41] shows a giant birefringence over 1.4. [29, 34, 38] Therefore, by incorporating MoS_2 into the design of PSR, its high refractive index would enhance the optical confinement and its extreme birefringence would improve the coupling efficiency between the two parallel waveguides, enabling a significant reduction in component footprint.

In this paper, we propose a concept of van der Waals on insulator (vdW-OI) configuration, in which two-dimensional (2D) materials are integrated into a layered stack with an insulating material, typically silicon dioxide (SiO_2). By utilizing this configuration, we design an ultra-compact and high-performance PSR based on ADC consisting of two parallel straight MoS_2 waveguides. Initially, we unveil the remarkable modal birefringence between the TE_0 and TM_0 modes of the MoS_2 waveguide by precisely calculating the effective refractive indices at the wavelength λ = 1.55 μm. Then, we demonstrate that the PSR can realize polarization separation and rotation with an ultra-small footprint. To the best of our knowledge, this is the simplest PSR design that can achieve high polarization conversion efficiency and ultra-short coupling length simultaneously. Through further simulations, we confirm the indispensability of the extremely birefringent MoS_2 waveguides in the realization of a simplistic yet ultra-compact PSR.

II. METHODS

Optical simulations are conducted with the lumerical software. MoS_2 is considered lossless and the imaginary parts of its refractive indices are set to zero, while the real parts are 4.07 and 2.7 for the in- and out-of-plane directions, respectively [34]. Other materials are selected from the material library of the simulation software.

III. RESULTS AND DISCUSSION

The proposed PSR is sketched in Fig. 1(a). It consists of an ADC with two parallel straight waveguides, an S-bend connected to the thru port, and the air upper cladding. The inset of Fig. 1(a) shows the layer structure of MoS_2 leading to its significant optical anisotropy. [42] To determine the cross-sectional sizes of the straight waveguides, we analyze the modal dispersions of MoS_2 waveguide using the mode solver integrated with the Finite-Difference Time-Domain (FDTD) software. [43] Fig. 1(b) illustrates the variation of the effective refractive indices (n_{eff}) of the first three guided modes with the increasing width of MoS_2 waveguide. Significantly, an extreme modal birefringence can be observed between the TM_0 and TE_0 modes (over 1.6), thereby offering a method for polarization separation. By adjusting the widths (W_1 and W_2) of these two straight waveguides, it becomes possible to achieve a phase-matching condition wherein the n_{eff} of the TM_0 mode in the thru waveguide matches that of the TE_0 mode in the cross waveguide. ($n_{\mathrm{eff}}^{1,\mathrm{TM}} = n_{\mathrm{eff}}^{2,\mathrm{TE}}$). To fulfill this condition, we employ structural parameters of W_1 = 455 nm and W_2 = 234 nm, thereby ensuring a modal birefringence larger than 1.4 in the thru waveguide. Consequently, the n_{eff} of TE_0 mode in the thru waveguide significantly deviates from that of any guided mode in the cross waveguide. Based on the coupled mode theory, this configuration guarantees uncoupled propagation for the TE_0 mode in the thru waveguide, [11, 44] while effectively facilitating the coupling of the TM_0 input mode to the adjacent cross waveguide through the ADC. As a result, simultaneous polarization separation and rotation are accomplished.

To ensure comparability with silicon-based straight waveguides ADC-PSR, [11] we maintain the same gap width between the two straight waveguides (W_g = 150 nm). By utilizing 3D lumerical FDTD simulations, we optimize the coupling length (L_c) based on the transmission performance of cross port and thru port. Fig. 2(a) illustrates the transmission coefficient as a function of L_c. Within the range of 5.6 to 6.8 μm, the PSR demonstrates a transmission efficiency higher than -0.4 dB for TM_0 to TE_0. Notably, at the L_c of 6.0 μm, the transmission efficiency of TM_0 to TE_0 achieves a peak value of -0.35 dB, while the transmission efficiency of TM_0 to TM_0 is -15.98 dB. With the optimized L_c, we perform simulations to analyze the optical power distribution of TM_0 and TE_0 polarized light along the waveguides, as shown in Fig. 2(b) and (c). For the TM_0 input mode [in Fig. 2(b)], the optical power in the thru waveguide gradually couples into the cross waveguide along the propagation direction, accompanied by conversion from TM_0 to TE_0 mode. The electric field distribution at the corresponding position in Fig. 2(d-f) further confirms the polarization conversion. Conversely, due to the significant modal birefringence of MoS_2 waveguide, a substantial phase mismatch exists between TE_0 mode in the thru waveguide and TE_0 mode in the cross waveguide. Consequently, the TE_0 input mode remains confined within the thru waveguide without any cross-coupling [Fig. 2(c)]. Thus, the simulation results validate the polarization separation and conversion functionalities of the proposed PSR.

To evaluate the performance of the designed PSR, we conduct 3D-FDTD simulations and calculate a series of key performance indicators. For the TM_0 input mode, a key parameter is the polarization conversion efficiency (PCE), defined as: [8]

$$PCE(\%) = T_{\mathrm{TE-cross}}/(T_{\mathrm{TE-cross}} + T_{\mathrm{TM-thru}}) \times 100\% \qquad (1)$$

where $T_{\mathrm{TE\text{-}cross}}$ is the transmission of TE_0 in the cross port and $T_{\mathrm{TM\text{-}thru}}$ is the transmission of TM_0 in the thru port. [26]

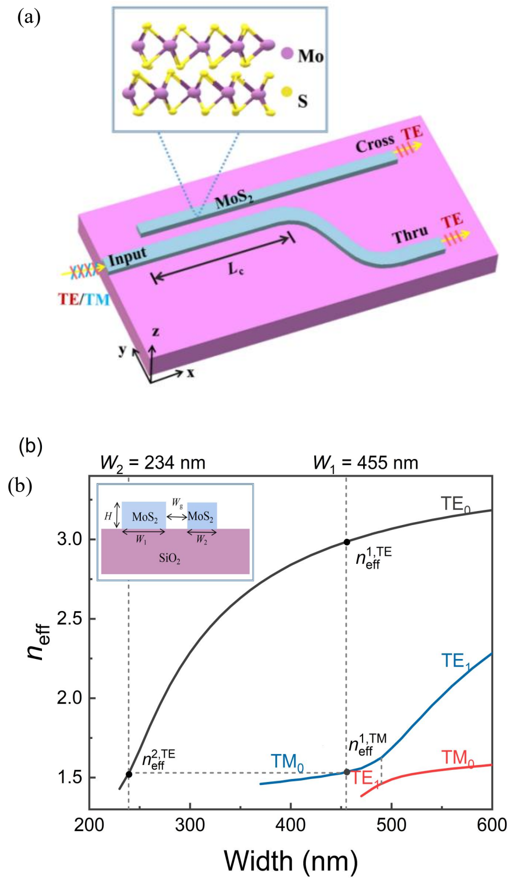

Fig. 1. Schematic diagram of the proposed PSR and modal characteristics of MoS_2 waveguide. (a) Layout of the MoS_2-based PSR, including two parallel straight waveguides an S-bend connected to the thru port, and the air upper cladding. L_c: the length of ADC. Inset: the layer structure of MoS_2. (b) Effective refractive indices (n_{eff}) of the first three guided modes in MoS_2 waveguide with varying width. H = 220 nm, λ = 1.55 μm. Inset: cross-section of the coupling region. W_1: width of thru waveguide. W_2: width of cross waveguide. W_g: width of the gap between two parallel coupled straight waveguides.

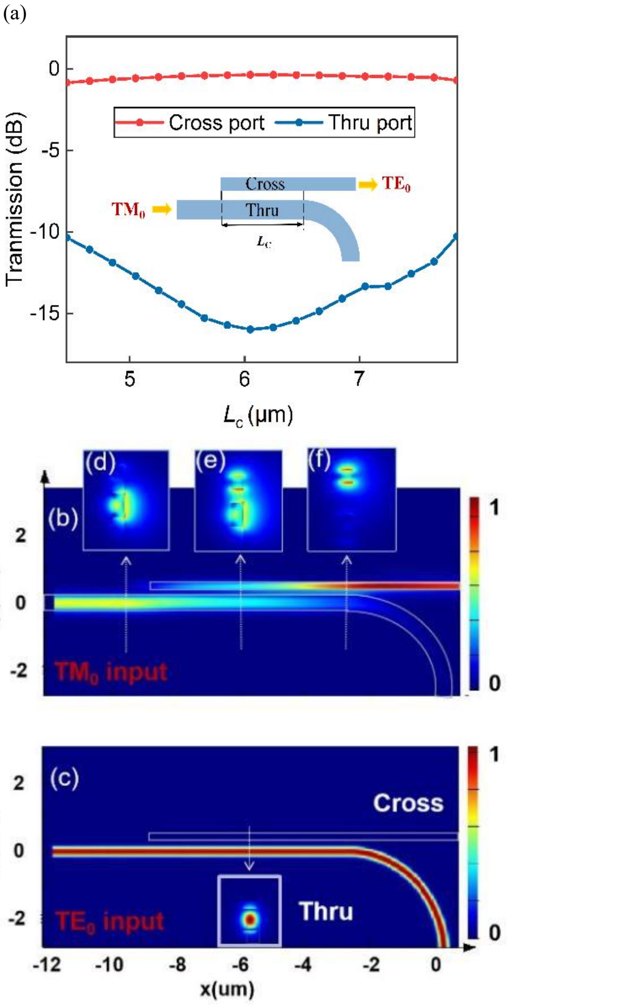

Fig. 2. Transmission characteristics of MoS_2-based PSR with different L_c and the optical power distribution in the PSR with W_1 = 455 nm, W_2 = 234 nm, H = 220 nm, and λ = 1.55 μm. (a) For TM_0 input mode, the transmission performance of the device varies with L_c. Inset: the simulation model. Optical power distribution in the designed PSR for (b) TM_0 input; (c) TE_0 input, inset: normalized electric field distribution with TE_0 as input. (d-f) TM_0 input, normalized electric field distributions at corresponding positions (indicated by arrows) along the PSR.

In addition, we also characterize the polarization conversion loss (*PCL*) and the crosstalk (*CT*), which are defined as:

$$PCL\ (\mathrm{dB}) = -10\log_{10}\frac{P_{\mathrm{TE}}^{\mathrm{C}}}{P_{\mathrm{TM}}^{\mathrm{I}}}, \tag{2}$$

$$CT\ (\mathrm{dB}) = 10\log_{10}\frac{P_{\mathrm{TM}}^{\mathrm{T}}}{P_{\mathrm{TE}}^{\mathrm{C}}}. \tag{3}$$

where refers to the power of the x polarization mode (TE or TM) at the y port (I: input port, T: thru port, C: cross port, and R: reflection port). [25] For the TE_0 input mode, we calculate *CT*, insertion loss (*IL*), and reflection loss (*RL*) instead, which are defined as: [25]

$$CT\ (\mathrm{dB}) = 10\log_{10}\frac{P_{\mathrm{TM}}^{\mathrm{C}}}{P_{\mathrm{TE}}^{\mathrm{T}}}, \tag{4}$$

$$IL\ (\mathrm{dB}) = -10\log_{10}\frac{P_{\mathrm{TE}}^{\mathrm{T}}}{P_{\mathrm{TE}}^{\mathrm{I}}}, \tag{5}$$

$$RL\ (dB) = 10\log_{10}\frac{P_{\mathrm{TE}}^{\mathrm{R}}}{P_{\mathrm{TE}}^{\mathrm{I}}}. \tag{6}$$

where the definition of is identical to that of the input TM_0 mode.

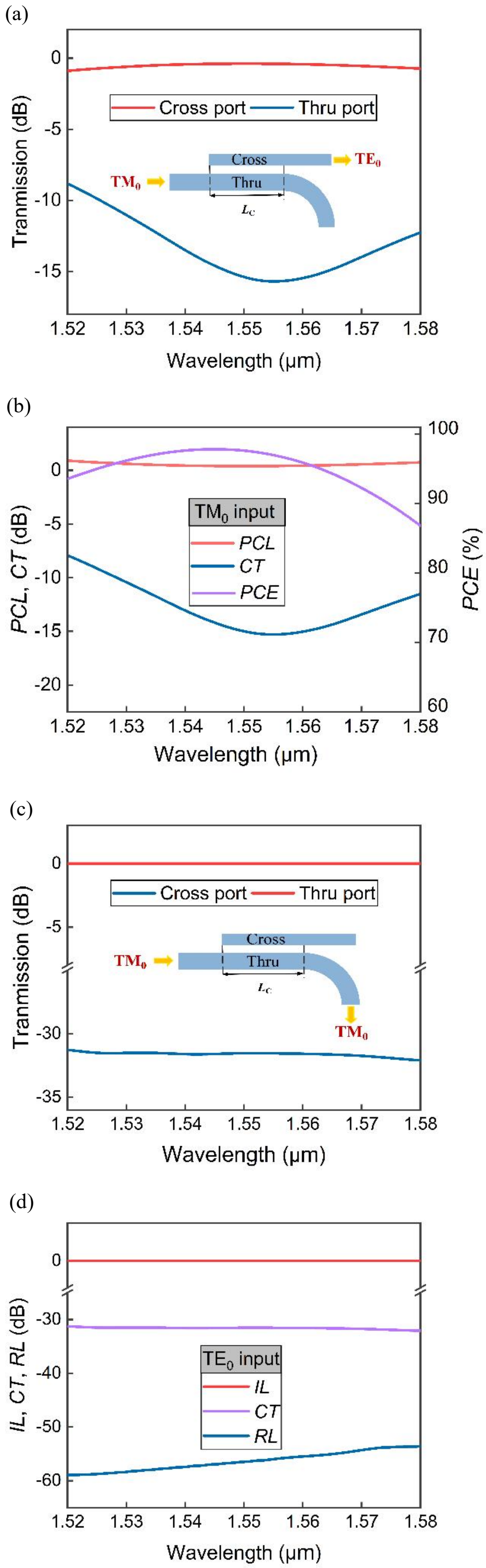

Fig. 3. Wavelength dependence of the key performance indicators (Transmission, *PCL*, *CT*, *PCE*, *IL* and *RL*) of the PSR. (a, b) TM_0 input and (c, d) TE_0 input. The simulation models are displayed in the insets respectively

Fig. 3 depicts the wavelength-dependent transmission performances of the designed PSR when TM_0 and TE_0 modes are used as inputs, respectively. With TM_0 as the input mode [Fig. 3(a)], the optical power output is mainly from the cross port, exhibiting wavelength dependence.

Specifically, the thru-port transmission reaches a minimum value of approximately -15.69 dB at λ = 1.55 μm, whereas the cross-port transmission reaches a maximum value of about -0.38 dB. Simultaneously, the *PCE* of TM_0 to TE_0 at the cross port achieves 96.97% [Fig. 3(b)], with the corresponding *CT* and *PCL* are -15.3 dB and 0.38 dB, respectively. As the working wavelength deviates from 1.55 μm, the *PCE* gradually decreases, meaning that TM_0 mode is sensitive to variations in wavelength. On the other hand, with TE_0 as the input mode [Fig. 3(c)], the optical power output primarily originates from the thru port and almost no light transmits into the cross waveguide, showing a wavelength-insensitive low *CT* of below -31 dB [as shown in Fig.3(d)]. This merit can be attributed to the extreme birefringence of MoS_2, which induces a significant phase mismatch between TE_0 mode in the thru waveguide and TE_0 mode in the cross waveguide. Furthermore, Fig. 3(d) also demonstrates that the TE_0 input mode has an exceptionally low *IL* of 0.006 dB and *RL* below -53 dB.

To explore the influence of MoS_2 birefringence on the coupling length and the key performance indicators of the PSR, we performed two sets of simulations, varying the out-

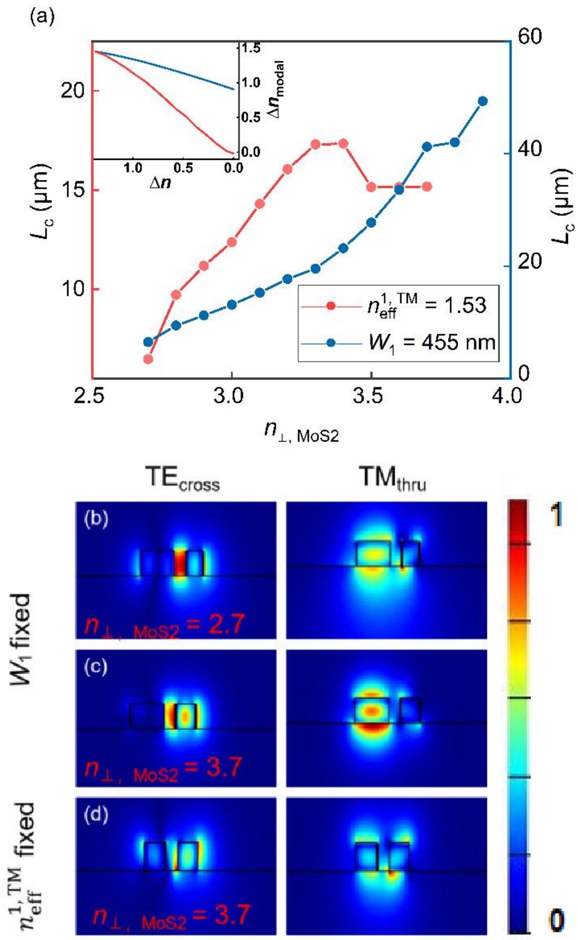

Fig. 4. Effect of the MoS_2 optical anisotropy on the coupling length of PSR. (a) Relationship between L_c and $n_{\perp,\ MoS2}$, with fixing $n_{eff}^{1,TM}$ =1.53 or W_1 = 455 nm. Inset: variation of the modal birefringence with $n_{\perp,\ MoS2}$ increase. Red: $n_{eff}^{1,TM}$ = 1.53; Blue: W_1 = 455 nm. Normalized electric field distributions of TE_{cross} and TM_{thru} in the ADC parallel straight waveguides with (b-c) W_1 = 455 nm and (d) $n_{eff}^{1,TM}$ = 1.53.

of-plane refractive index of MoS_2 ($n_{\perp,\ MoS2}$) while fixing W_1 = 455 nm and $n_{eff}^{1,TM}$ =1.53, respectively. As shown in Fig. 4(a), the coupling length exhibits a nonlinear increase with increasing $n_{\perp,\ MoS2}$ (the variations of modal birefringence are shown in the inset). Particularly, at W_1 = 455 nm, L_c exponentially increases from 6 μm ($n_{\perp,\ MoS2}$ = 2.7) to 49.4 μm ($n_{\perp,\ MoS2}$ = 3.9), where $n_{\perp,\ MoS2}$ = 2.7 is the genuine out-of-plane refractive index of MoS_2. This arises from the enhanced field confinement capability of the input waveguide (as demonstrated in Fig. 4(b, c)), resulting from the increased value of $n_{eff}^{1,TM}$. Consequently, there is a reduction in modal field overlap between the coupled waveguides, leading to a weakened cross-coupling effect. [45] However, when $n_{eff}^{1,TM}$ = 1.53, L_c varies non-monotonically. This intricate behaviour arises from the interplay of two factors influencing the cross-coupling strength. Firstly, the decrease in optical birefringence diminishes the cross-coupling owing to alterations in the polarization fraction of TM_0 and TE_0 in the eigenmodes. Secondly, the reduction of W_1 increases the modal field overlap, thereby reinforcing the cross-coupling effect. In general, the reduction of birefringence exerts a more pronounced influence on cross-coupling, resulting in an elongation of the coupling length. However, when W_1 is small enough (<300 nm), a greater portion of the modal fields extends beyond the waveguide boundaries (e. g. in Fig. 4(d), W_1 = 267 nm), thereby amplifying the modal field overlap. It is the delicate balance between these opposing factors that give rise to the non-monotonical behavior observed in L_c illustrated in Fig. 4(a).

The key performance indicators of the PSR are also birefringence-dependent. With TE_0 as input mode, the *CT* between the adjacent waveguides sharply enlarged with the increase of $n_{\perp,\ MoS2}$ at $n_{eff}^{1,TM}$ = 1.53, as depicted in Fig. 5(a). Specifically, when $n_{\perp,\ MoS2}$ = 3.7, *CT* is as high as -5.6 dB, and the corresponding *IL* exceeds 1 dB. When W_1 = 455 nm, the increase of $n_{\perp,\ MoS2}$ has little effect on the transmission performance of the device [Fig. 5(b)]. This phenomenon can be attributed to the reduced optical birefringence (modal birefringence), which diminishes the phase mismatch between TE_0 in the thru waveguide and TE_0 in the cross waveguide. Notably, fixing $n_{eff}^{1,TM}$ = 1.53 results in a significantly lower modal birefringence compared to fixing W_1 = 455 nm as shown in Fig. 4(a) insert. For instance, when the phase matching condition is satisfied at $n_{eff}^{1,TM}$ = 1.53 and $n_{\perp,\ MoS2}$ = 3.7, the waveguide widths are optimized to W_1 = 267 nm and W_2 = 250 nm, respectively. However, the corresponding modal birefringence is merely 0.36, which is far less than 1.4 observed at $n_{\perp,\ MoS2}$ = 2.7. Consequently, a portion of the optical energy couples into the adjacent waveguide, leading to an increase in insertion loss and mode crosstalk [Fig. 5(a) inset]. On the other hand, with TM_0 as input mode [Fig. 5(c, d)], regardless of the values of $n_{eff}^{1,TM}$= 1.53 or W_1 = 455 nm, effective conversion of TM_0 to TE_0 can be achieved by satisfying the phase matching condition. However, the transmission coefficients noticeably decrease at low birefringence levels. Hence, the extreme birefringence of MoS_2 is crucial to realize an ultra-compact PSR with high transmission performance.

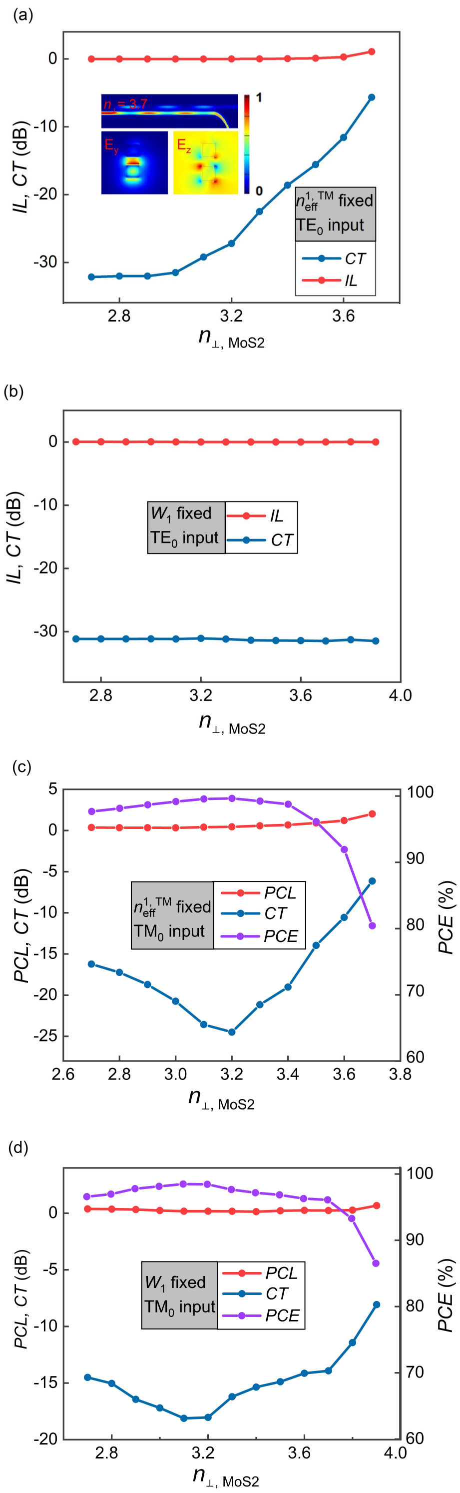

Fig. 5. Influence of MoS_2 birefringence on the transmission performance of PSR. *CT* and *IL* of the PSR with the variation of $n_{\perp,\mathrm{MoS2}}$ in TE_0 input mode: (a) $n_{\mathrm{eff}}^{1,\mathrm{TM}}$ =1.53 Inset: when $n_{\mathrm{eff}}^{1,\mathrm{TM}}$ = 1.53 and $n_{\perp,\mathrm{MoS2}}$ = 3.7, the optical power distribution in the designed PSR, and the normalized electric field distribution (E_y and E_z) diagram of the cross-section of ADC. (b) W_1 = 455 nm. The *PCE*, *PCL* and *CT* of the PSR with the variation of $n_{\perp,\mathrm{MoS2}}$ in TM_0 input mode: (c) $n_{\mathrm{eff}}^{1,\mathrm{TM}}$ = 1.53. (d) W_1 = 455 nm. W_g = 150 nm.

IV. Conclusions

An ultra-compact and high-performance PSR based on the vdW-OI configuration is conceptually proposed and numerically demonstrated in this work. Due to the large modal birefringence between TE_0 and TM_0 modes in the thru waveguide, the TE-TE coupling is suppressed while the TM-TE coupling can be of high efficiency. As a result, polarization conversion from TM_0 to TE_0 can be achieved within a coupling length as small as 6.0 μm with a high *PCE* of 96.97% and a low *PCL* of 0.38 dB (λ = 1.55 μm). At the same time, the *IL* and the *CT* for the TE_0 input mode are both extremely low (0.006 dB and -31.53 dB, respectively). We emphasize that both the ultra-compact size and the improved performances of our design stem from the giant birefringence exhibited by MoS_2. Therefore, our utilization of highly birefringent materials offers a promising strategy for density integration of polarization management devices based on vdW-OI configuration. Regarding practical fabrication, a device size less than 10 μm would greatly relax the requirement for large-sized single crystals thus mechanically exfoliated MoS_2 flakes are quite adequate.

Acknowledgment

This work is supported by the National Basic Key Research Program of China (2020YFB2206103). D.H. acknowledges the support from the National Natural Science Foundation of China (52072083) and the Youth Innovation Promotion Association of CAS.

References

[1] S. Mao, L. Cheng, C. Zhao and H. Y. Fu, “Ultra-broadband and ultra-compact polarization beam splitter based on a tapered subwavelength-grating waveguide and slot waveguide,” Opt. Express, vol. 29, pp. 28066-28077, 2021.

[2] Y. Tian, J. Qiu, C. Liu, S. Tian, Z. Huang and J. Wu, “Compact polarization beam splitter with a high extinction ratio over S + C + L band,” Opt. Express, vol. 27, pp. 999-1009, 2019.

[3] Y. Bian, L. Kang, Q. Ren, Y. Zheng, R. Engel-Herbert, P. L. Werner, et al., "Hybrid vanadate waveguiding configurations for extreme optical confinement and efficient polarization management in the near-infrared," Nanoscale, vol. 10, pp. 16667-16674, 2018.

[4] Y. Kim, D. W. Kim, M.-H. Lee, M. H. Lee, D. E. Yoo, K. N. Kim, et al., “Demonstration of integrated polarization rotator based on an asymmetric silicon waveguide with a trench,” J. Opt., vol. 18, p. 095801, 2016.

[5] W. Bogaerts, R. Baets, P. Dumon, V. Wiaux, S. Beckx, D. Taillaert, et al., “Nanophotonic waveguides in silicon-on-insulator fabricated with CMOS technology,” J. Lightwave Technol., vol. 23, pp. 401-412, 2005.

[6] D. Dai, L. Liu, S. Gao, D.-X. Xu and S. He, “Polarization management for silicon photonic integrated circuits,” Laser Photonics Rev., vol. 7, pp. 303-328, 2013.

[7] W. Bogaerts, M. Fiers and P. Dumon, “Design challenges in silicon photonics,” IEEE J. Sel. Top. Quantum Electron., vol. 20, pp. 1-8, 2014.

[8] H. Subbaraman, X. Xu, A. Hosseini, X. Zhang, Y. Zhang, D. Kwong, et al., “Recent advances in silicon-based passive and active optical interconnects,” Opt. Express, vol. 23, pp. 2487-2510, 2015.

[9] B. Bai, L. Liu and Z. Zhou, “Ultracompact, high extinction ratio polarization beam splitter-rotator based on hybrid plasmonic-dielectric directional coupling,” Opt. Lett., vol. 42, pp. 4752-4755, 2017.

[10] D. Dai and J. E. Bowers, “Novel concept for ultracompact polarization splitter-rotator based on silicon nanowires,” Opt. Express, vol. 19, pp. 10940-10949, 2011.

[11] L. Liu, Y. Ding, K. Yvind and J. M. Hvam, “Silicon-on-insulator polarization splitting and rotating device for polarization diversity circuits,” Opt. Express, vol. 19, pp. 12646-12651, 2011.

[12] X. Ruan, H. Li, and T. Chu, "Inverse-designed ultra-compact polarization splitter–rotator in standard silicon photonic platforms with large fabrication tolerance," Journal of Lightwave Technology, vol. 40, pp. 7142-7149, 2022.

[13] K. Tan, Y. Huang, G.-Q. Lo, C. Yu and C. Lee, “Experimental realization of an O-band compact polarization splitter and rotator,” Opt. Express, vol. 25, pp. 3234-3241, 2017.

[14] Y. Zhang, Y. He, X. Jiang, B. Liu, C. Qiu, Y. Su, et al., "Ultra-compact and highly efficient silicon polarization splitter and rotator," APL Photonics, vol. 1, p. 091304, 2016.

[15] Y. Ding, H. Ou, and C. Peucheret, "Wideband polarization splitter and rotator with large fabrication tolerance and simple fabrication process," Opt. Lett., vol. 38, pp. 1227-1229, 2013.

[16] H. Guan, A. Novack, M. Streshinsky, R. Shi, Q. Fang, A. E. Lim, et al., "Baehr-Jones and M. Hochberg, "CMOS-compatible highly efficient polarization splitter and rotator based on a double-etched directional coupler," Opt. Express, vol. 22, pp. 2489-2496, 2014.

[17] W. D. Sacher, T. Barwicz, B. J. Taylor and J. K. Poon, "Polarization rotator-splitters in standard active silicon photonics platforms," Opt. Express, vol. 22, pp. 3777-3786, 2014.

[18] J. Wang, B. Niu, Z. Sheng, A. Wu, W. Li, X. Wang, et al., "Novel ultra-broadband polarization splitter-rotator based on mode-evolution tapers and a mode-sorting asymmetric Y-junction," Opt. Express, vol. 22, pp. 13565-13571, 2014.

[19] J. Wang, M. Qi, Y. Xuan, H. Huang, Y. Li, M. Li, et al., "Proposal for fabrication-tolerant SOI polarization splitter-rotator based on cascaded MMI couplers and an assisted bi-level taper," Opt. Express, vol. 22, pp. 27869-27879, 2014.

[20] B. Qiu, X. Zhao, G. Hu, W. Yue, J. Ren, and X. Yuan, "Optical properties of graphene/MoS_2 heterostructure: first principles calculations," Nanomaterials (Basel), vol. 8, 2018.

[21] T. Hu, M. S. Rouifed, H. Qiu, X. Guo, C. G. Littlejohns, C. Liu, et al., "A polarization splitter and rotator based on a partially etched grating-assisted coupler," IEEE Photonics Technol. Lett., vol. 28, pp. 911-914, 2016.

[22] M. Ma, A. H. K. Park, Y. Wang, H. Shoman, F. Zhang, N. A. F. Jaeger, et al., "Sub-wavelength grating-assisted polarization splitter-rotators for silicon-on-insulator platforms," Opt. Express, vol. 27, pp. 17581-17591, 2019.

[23] Y. Wang, M. Ma, H. Yun, Z. Lu, X. Wang, N. A. F. Jaeger, et al., "Ultra-compact sub-wavelength grating polarization splitter-rotator for silicon-on-insulator platform," IEEE Photonics J., vol. 8, pp. 1-9, 2016.

[24] B. Bai, L. Pei, J. Zheng, T. Ning and J. Li, "Ultra-short plasmonic polarization beam splitter-rotator using a bent directional coupler," Chinese Opt. Lett., vol. 18, p. 041301, 2020.

[25] H. Xu, D. Dai and Y. Shi, "Ultra-broadband and ultra-compact on-chip silicon polarization beam splitter by using hetero-anisotropic metamaterials," Laser Photonics Rev., vol. 13, p. 1800349 , 2019.

[26] T. Zhang, X. Ke, X. Yin, L. Chen and X. Li, "Graphene-assisted ultra-compact polarization splitter and rotator with an extended bandwidth," Sci. Rep., vol. 7, 12169, 2017.

[27] Y. Xu and J. Xiao, "Ultracompact and high efficient silicon-based polarization splitter-rotator using a partially-etched subwavelength grating coupler," Sci. Rep., vol. 6, p. 27949, 2016

[28] X. Han, Y. Jiang, A. Frigg, H. Xiao, P. Zhang, T. G. Nguyen, et al., "Mode and polarization-division multiplexing based on silicon nitride loaded lithium niobate on insulator platform," Laser Photonics Rev., vol. 16, p. 2100529, 2021.

[29] G. A. Ermolaev, D. V. Grudinin, Y. V. Stebunov, K. V. Voronin, V. G. Kravets, J. Duan, et al., "Giant optical anisotropy in transition metal dichalcogenides for next-generation photonics," Nat. Commun., 12(1), 854 (2021).

[30] Z. Fei, M. E. Scott, D. J. Gosztola, J. J. Foley, J. Yan, D. G. Mandrus, et al., "Nano-optical imaging ofWSe2waveguide modes revealing light-exciton interactions," Phys. Rev. B, vol. 94, p. 081402, 2016.

[31] D. Hu, X. Yang, C. Li, R. Liu, Z. Yao, H. Hu, et al., "Probing optical anisotropy of nanometer-thin van der Waals microcrystals by near-field imaging," Nat. Commun. vol. 8, p. 1471, 2017.

[32] F. Hu, Y. Luan, M. E. Scott, J. Yan, D. G. Mandrus, X. Xu, et al., "Imaging exciton–polariton transport in $MoSe_2$ waveguides," Nat. Photonics., vol. 11, pp. 356-360, 2017.

[33] B. Munkhbat, P. Wrobel, T. J. Antosiewicz and T. O. Shegai, "Optical constants of several multilayer transition metal dichalcogenides measured by spectroscopic ellipsometry in the 300-1700 nm range: high index, anisotropy, and hyperbolicity," ACS Photonics, vol. 9, pp. 2398-2407, 2022.

[34] B. Munkhbat, B. Kucukoz, D. G. Baranov, T. J. Antosiewicz and T. O. Shegai, "Nanostructured transition metal dichalcogenide multilayers for advanced nanophotonics," Laser Photonics Rev., vol. 17, p. 2200057, 2022.

[35] H. Ling, J. B. Khurgin, and A. R. Davoyan, "Atomic-void van der Waals channel waveguides," Nano Letters, vol. 22, pp. 6254-6261, 2022.

[36] H. Ling, R. Li, and A. R. Davoyan, "All van der Waals integrated nanophotonics with bulk transition metal dichalcogenides," ACS Photonics, vol. 8, pp. 721-730, 2021.

[37] V. E. Babicheva, S. Gamage, L. Zhen, S. B. Cronin, V. S. Yakovlev and Y. Abate, "Near-field surface waves in few-layer MoS_2," ACS Photonics, vol. 5, pp. 2106-2112, 2018.

[38] D. Hu, K. Chen, X. Chen, X. Guo, M. Liu and Q. Dai, "Tunable modal birefringence in a low-loss van der Waals waveguide," Adv. Mater. vol. 31, p. 180778, 2019.

[39] Y. Li, A. Chernikov, X. Zhang, A. Rigosi, H. M. Hill, A. M. van der Zande, et al., "Measurement of the optical dielectric function of monolayer transition-metal dichalcogenides: MoS_2, $MoSe_2$,WS_2, and WSe_2," Phys. Rev. B, vol. 90, p. 205422, 2014.

[40] R. Verre, D. G. Baranov, B. Munkhbat, J. Cuadra, M. Kall and T. Shegai, "Transition metal dichalcogenide nanodisks as high-index dielectric Mie nanoresonators," Nat Nanotechnol., vol. 14, pp. 679-683, 2019.

[41] G. A. Ermolaev, Y. V. Stebunov, A. A. Vyshnevyy, D. E. Tatarkin, D. I. Yakubovsky, S. M. Novikov, et al., "Broadband optical properties of monolayer and bulk MoS_2," npj 2D Mater. and Appl., vol. 4, p. 21, 2020.

[42] K. S. Novoselov, A. Mishchenko, A. Carvalho and A. H. Castro Neto, "2D materials and van der Waals heterostructures," Science, vol. 353, p. aac9439, 2016.

[43] T. Kamalakis, D. Alexandropoulos and N. Vainos, "Efficient design of polymer micro-ring resonator filters based on coupled mode theory and finite difference mode solver," Opt. Commun., vol. 339, pp. 123-128, 2015 .

[44] D. Grudinin, O. Matveeva, G. Ermolaev, A. Vyshnevyy, A. Arsenin, and V. Volkov, "Reduction in crosstalk between integrated anisotropic optical waveguides," Photonics, vol. 10, p. 59, 2023.

[45] Z. Wang, N. Zhu, Y. Tang, L. Wosinski, D. Dai and S. He, "Ultracompact low-loss coupler between strip and slot waveguides," Opt. Lett., vol. 34, pp. 1498-1500, 2009.